

Replicating weak-lensing summary-statistic covariances with normalizing flows

Joaquin Armijo,^{1, 2, *} Leander Thiele,¹ and Jia Liu¹

¹*Center for Data-Driven Discovery, Kavli IPMU (WPI), UTIAS,
The University of Tokyo, Kashiwa, Chiba 277-8583, Japan*

²*Department of Mathematical Physics, Institute of Physics,
University of São Paulo, R. do Matão 1371, 05508-090, São Paulo, SP, Brazil*

We explore the ability of normalizing flow (NF) generative models to reproduce weak-lensing summary statistics when trained on a set of cosmological simulations. Our analysis focuses on how accurately NF models recover the mean, standard deviation, and covariance of key statistics derived from convergence (κ) maps: The angular power spectrum C_ℓ , probability density function, and Minkowski functionals of weak lensing convergence κ -maps. We test two scenarios for training: (1) on the data vectors and (2) on the full κ -maps. In both cases, the NF models reproduce the mean and variance of the target statistics within percent-level accuracy. However, the accuracy of the off-diagonal elements of the covariance matrix is underestimated by up to $\sim 25\%$. We study several mitigation strategies and find that data augmentation and training with noisy fields help improve covariance recovery to $\mathcal{O}(10\%)$. Our study demonstrates that while the means and variances of weak lensing statistics can be well modeled by NF, covariances can be significantly underestimated if mitigation strategies are not applied.

I. INTRODUCTION

Weak gravitational lensing is a powerful observational tool that probes the large-scale distribution of matter in the universe. It arises from the subtle distortion of the shapes of distant galaxies due to the gravitational influence of intervening mass along the line of sight [1–3]. By statistically analyzing these distorted shapes across a large sample of galaxies, the distribution of matter can be inferred and studied over cosmic history. This makes weak lensing a key probe for inferring cosmological parameters, such as the matter energy-density Ω_m , the amplitude of matter fluctuations σ_8 , and the properties of dark energy [4, 5], thereby offering critical insights into the fundamental nature of the universe.

Weak lensing fields are designed through observations of large extragalactic surveys, such as the Dark Energy Survey (DES) [6], the Kilo-degree survey [7], the Hyper Suprime-Cam (HSC) [8], and upcoming ones, such as Euclid [9] and Vera C. Rubin Observatory Legacy Survey of Space and Time (LSST) [10] missions. These experiments have observed millions of distant galaxies across vast areas of the sky, enabling the creation of lensing catalogs by precisely measuring the cosmic shear of individual galaxies. From these shape measurements, the projected mass density can be reconstructed [11], allowing researchers to produce detailed maps of the underlying matter distribution.

Cosmological simulations are essential for modeling the late-time matter field and generating mock universes with gravitational lensing effects [12]. These simulations help to test mass-mapping techniques [13–15], model observational systematics [16], interpreting cosmic shear data [17], and including the effect of baryons [18], ultimately improving our ability to constrain cosmological

models. However, producing large ensembles that simulate the large volume and high-resolution of the data remains computationally expensive and has become a major bottleneck for weak-lensing analyses. Machine-learning-based generative models offer a promising path forward. Methods such as VAEs, GANs, NFs, and diffusion models can learn the non-Gaussian structure of weak-lensing convergence maps directly from simulations [19–26]. Once trained, these models can generate high-fidelity synthetic κ -maps at negligible computational cost, reproducing both standard and higher-order statistics [27]. This enables extensive mock catalog production, exploration of rare events, and scalable uncertainty quantification. When conditioned on cosmological parameters, they additionally serve as fast emulators for cosmological inference [22, 28, 29], providing a data-driven complement to traditional simulation pipelines.

In this work, we study flow-based generative models as a flexible and interpretable framework for modeling weak-lensing convergence maps generated by cosmological simulations. Normalizing flows (NFs) learn an invertible mapping between a multivariate Gaussian latent space and the target data distribution, providing an explicit and tractable likelihood and avoiding mode collapse, in contrast to adversarial approaches [23, 30]. When trained on suites of simulations, NFs approximate the probability distribution of convergence fields and enable the generation of large ensembles of high-fidelity synthetic maps with the same dimensionality as the original data. Given the variable performance of neural networks in cosmological applications, their validity must be assessed by how accurately they reproduce key summary statistics and utilize the available training information. We apply NFs to two-dimensional convergence (κ) fields, which are line-of-sight projections of the matter density, and evaluate statistical fidelity using complementary probes: the angular power spectrum $C_\ell^{\kappa\kappa}$, which captures Gaussian information, the one-point κ probability distribution func-

* joaquin.armijo@usp.br

tion, which probes higher-order moments, and Minkowski functionals, which characterize the topology of the field.

This paper is organized as follows: We describe weak lensing, including convergence fields and their summary statistics in section II. The simulations used to train the neural network are described in Section III. A description of normalizing flow networks is written in Section IV. We show and discuss the results of the replication of summary statistics in V. Finally, conclusions are drawn in Section VI.

II. WEAK LENSING

The deflection of extragalactic background source light by a gravitational potential leads to coherent distortions in the observed galaxy shape, a phenomenon known as cosmic shear. The weak lensing effect is described by the Jacobian matrix \mathcal{A} , which relates the unlensed position of a light ray to its observed (lensed) position:

$$\mathcal{A} = \begin{pmatrix} 1 - \kappa - \gamma_1 & -\gamma_2 \\ -\gamma_2 & 1 - \kappa + \gamma_1 \end{pmatrix} \quad (1)$$

where κ denotes the convergence, which captures the isotropic magnification of images, and $\gamma = \gamma_1 + i\gamma_2$ is the complex *shear*, responsible for the anisotropic distortion of galaxy shapes. In the weak-lensing regime, where $|\kappa|, |\gamma| \ll 1$, the lensing transformation is well described by a linear approximation. Since the lensing-induced shear of any individual galaxy is much smaller than its intrinsic shape noise, the signal must be statistically recovered by averaging over large ensembles of galaxies.

The convergence κ is of particular interest because it directly relates to the projected matter density along the line of sight. It is defined as a weighted integral of the three-dimensional matter overdensity field δ :

$$\kappa(\boldsymbol{\theta}) = \int_0^{\chi_s} d\chi W(\chi') \delta(\chi', \boldsymbol{\theta}), \quad (2)$$

where χ is the comoving distance, χ_s is the distance to the source galaxy, and $W(\chi)$ is the lensing efficiency kernel, given by:

$$W(\chi) = \frac{3H_0^2\Omega_m}{2c^2} \frac{\chi}{a(\chi)} \int_\chi^{\chi_s} d\chi' n(\chi') \frac{\chi' - \chi}{\chi'}, \quad (3)$$

with $n(\chi')$ being the source galaxy distribution, c the speed of light, $a(\chi)$ the scale factor, H_0 the Hubble constant, and Ω_m the matter density parameter.

Mapping the convergence field provides a two-dimensional view of the projected matter distribution, which includes both dark and baryonic matter. These convergence maps are key for studying the growth of cosmic structure and for inferring cosmological parameters.

Recent and ongoing weak lensing surveys have significantly advanced our ability to create high-fidelity convergence maps and perform statistical inference. The Dark Energy Survey (DES) [31], the Kilo-Degree Survey (KiDS) [32], and the Hyper Suprime-Cam (HSC) survey [33] have provided precise measurements of cosmic structure.

A. Summary statistics

Extracting cosmological information from weak-lensing convergence maps relies on summary statistics that quantify the spatial structure of the projected matter density field. Although κ is a line-of-sight projection of the underlying matter distribution, it becomes significantly non-Gaussian on small angular scales as a result of nonlinear gravitational evolution. Consequently, a broad range of summary statistics is employed to capture the information content of weak-lensing fields, spanning traditional two-point statistics and higher-order statistics providing significant non-Gaussian information.

Convergence Angular Power Spectrum

The angular power spectrum of the convergence field, $C_\ell^{\kappa\kappa}$, is the most widely used two-point statistic in weak lensing analyses. It quantifies the variance of two-dimensional density fluctuations as a function of angular scale ℓ , and is defined by the ensemble average of the spherical harmonic coefficients of the field:

$$\langle \kappa_{\ell m} \kappa_{\ell' m'}^* \rangle = \delta_{\ell\ell'} \delta_{mm'} C_\ell^{\kappa\kappa}, \quad (4)$$

where $\kappa_{\ell m}$ are the spherical harmonic coefficients of the convergence field $\kappa(\boldsymbol{\theta})$. This power spectrum is directly related to the 3D matter power spectrum $P_\delta(k)$ through the Limber approximation and carries information about the amplitude and scale dependence of matter fluctuations. Cosmological parameters such as $S_8 = \sigma_8 \sqrt{\frac{\Omega_m}{0.3}}$ can be constrained using measurements of $C_\ell^{\kappa\kappa}$.

Convergence Probability Distribution Function (PDF)

The power spectrum contains Gaussian information of the convergence field, including its variance. To study higher-order moments, the one-point probability distribution function (PDF) of the κ provides complementary information by encoding the full distribution of pixel values across the map containing information about the amplitude of the correlation functions of the field. The shape of the κ -PDF is sensitive to non-Gaussian features arising from nonlinear structure formation and includes contributions from higher-order moments like skewness and kurtosis [34–36].

The κ -PDF is particularly effective at probing the tails of the convergence distribution, which correspond to rare structures such as massive clusters (high κ) or two-dimensional voids (low κ). PDF measurements recover information of the amplitude of one-point fluctuations and, once combined with information inferred from the power spectrum, provide improved constraints in the S_8 cosmological parameter [37–39].

Minkowski Functionals

Minkowski functionals (MFs) are a set of morphological descriptors that quantify the topology and geometry of scalar fields like $\kappa(\theta)$. In two dimensions, there are three functionals: the area fraction V_0 , the perimeter length V_1 , and the Euler characteristic (or genus) V_2 , defined over excursion sets where the field exceeds a given threshold ν .

Mathematically, for a field κ and under a smoothing angular scale, the Minkowski functionals can be written as integrals over the excursion set:

$$V_0(\nu) = \frac{1}{A} \int_{\kappa > \nu} dA, \quad (5)$$

$$V_1(\nu) = \frac{1}{4A} \int_{\partial(\kappa > \nu)} dl, \quad (6)$$

$$V_2(\nu) = \frac{1}{2\pi A} \int_{\partial(\kappa > \nu)} dl \kappa_c, \quad (7)$$

where A is the total area of the field, $\partial(\kappa > \nu)$ denotes the boundary of the region where κ exceeds ν , and κ_c is the local curvature along this boundary.

Minkowski functionals are sensitive to both Gaussian and non-Gaussian features in the field and have been shown to outperform standard two-point statistics in some cases, especially in the nonlinear regime [40, 41]. Their ability to capture the shape, connectivity, and filamentary structure of the convergence field makes them a powerful tool for extracting cosmological information beyond the power spectrum.

Combined constraints of MFs and $C_\ell^{\kappa\kappa}$ improve the constraints of S_8 in comparison to the power spectrum alone by 40% [42].

Together, these summary statistics provide a multi-faceted description of the convergence field and are crucial for maximizing the scientific return of current and future weak lensing surveys. They are also instrumental in validating cosmological models and training data-driven methods such as machine learning emulators and likelihood-free inference techniques. [43–45]

III. SIMULATIONS

We model convergence field maps constructed from numerical simulations of galaxy cosmic shear. The SLICS

simulations [17] are a publicly available suite of high-resolution N -body simulations tailored specifically for weak lensing and large-scale structure analyses.

To study weak lensing effects and interpret observational data, it is essential to produce convergence maps to study the statistical and physical properties of the Universe. One widely used approach is through the multiple-plane tiling technique [13]. In the case of SLICS simulations, convergence is extracted using the Born approximation, where the deflection angles and shear tensors are computed from 18 mass sheets acting as the lens planes.

SLICS simulations provide a sample of $N_{\text{sims}} = 954$ independent light-cones of 10 deg^2 used to calculate the covariance matrix for stage-III surveys, such as KiDS, DES, and HSC. We will use these maps as training data for our machine learning model to test how well the summary statistic information can be learned.

IV. FLOW BASED NEURAL NETWORKS

Normalizing flow (NF) networks constitute a class of generative models that learn complex probability distributions by transforming a simple base distribution, such as a multivariate Gaussian, through a sequence of invertible and differentiable mappings. By defining a series of these bijective transformations, a flow maps a latent distribution $p(z)$ into a target data distribution $p(x)$ according to the change-of-variables rule. Each transformation is designed to be invertible, with a tractable Jacobian determinant, which allows exact likelihood evaluation and efficient sampling. Flow-based models can be implemented using various architectures, with defined transformations, offering a trade-off between expressiveness and computational efficiency. In contrast to generative adversarial networks (GANs) and variational autoencoders (VAEs), normalizing flows maintain an exact, one-to-one correspondence between the latent and data spaces, preserving dimensionality throughout the training process. In our task to replicate information from weak lensing κ fields, we focus in two types of architectures: Neural spline flows and multiscale flows.

A. Neural spline flow

Neural spline flow (NSF) networks are a class of normalizing flow models that employ a collection of polynomial splines to construct transformations for density estimation. By using rational–quadratic or higher-order spline functions, NSF enables flexible and invertible mappings between simple base Gaussian distribution and complex target distributions [46]. The splines are parameterized by neural networks, which predict the knot positions and derivatives, providing a data-dependent transformation at each layer. Combining the adaptability of splines, the NSF is helpful for the generative sampling and probabilistic modeling. For example, for learning

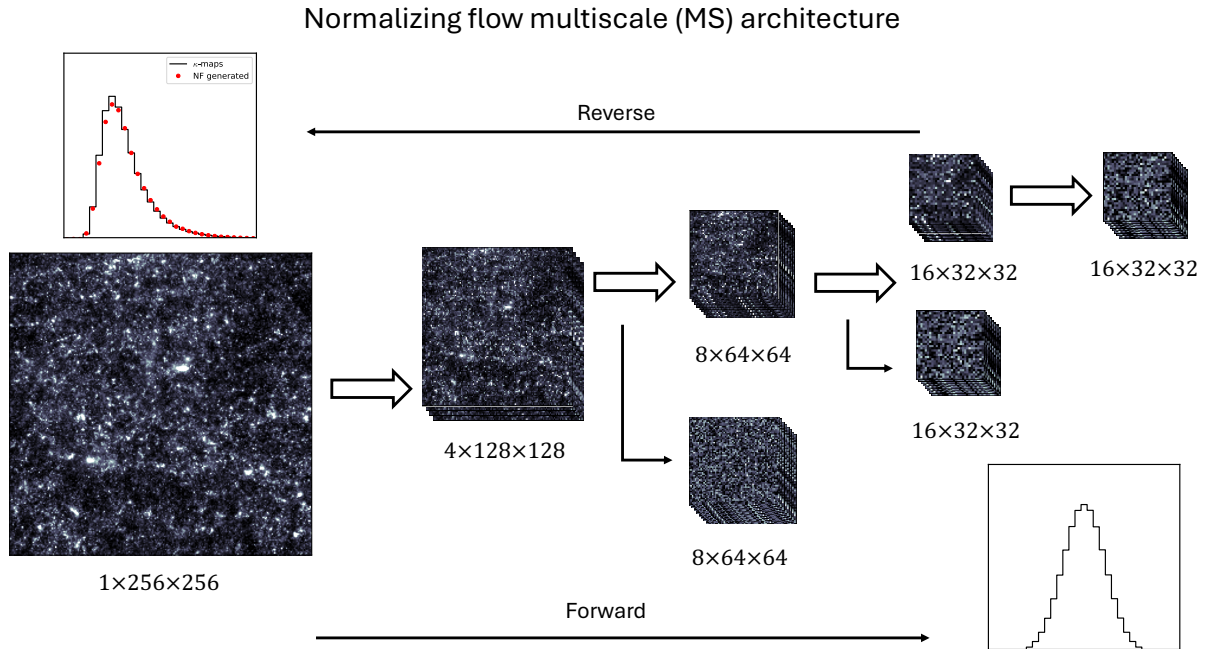


FIG. 1. Diagram of multiscale NF network used for learning κ -map features. Images are passed through the flow with an initial size of $N_{\text{pix}} = 256 \times 256$ with a clear non-Gaussian distribution. After all the transformation, the latent space represents a Gaussian random field with the same image dimensions (number of pixels). The image representation is schemed in the center, showing how the original image, a convergence map, loses resolution by passing coupling, squeezing, and splitting transforms until it becomes indistinguishable from Gaussian random noise. The nature of the NF network requires the flow to be invertible, allowing for the generation of κ -maps from an initial Gaussian random field.

the summary statistic of a set of simulations, we employ the NSF to replicate the likelihood distributions of weak-lensing summary statistics. The networks used to learn these target distributions are relatively compact, containing $N_{\text{par}} \simeq 3-4 \times 10^5$ trainable parameters. For our implementation, each model consists of five masked autoregressive flow (MAF), where each block defines collection of splines with a defined Jacobian determinant [47].

B. Multi-scale normalizing flow

Multiscale architectures in normalizing flows are designed to efficiently model the complex, hierarchical structure of image data by progressively transforming data at multiple spatial resolutions. Instead of processing the entire image at full resolution throughout the flow, these architectures split the data into different scales, typically by factoring out low-level details at earlier stages and modeling high-level structure in coarser representations [48, 49]. This strategy not only reduces computational costs but also improves modeling flexibility and sample quality, making it particularly effective for image generation tasks where capturing both global structure and fine-grained details is crucial. This particular architecture becomes relevant when studying κ -maps, as these follow the hierarchical large-scale structure, making it crucial for studying the convergence field.

In practice, this is the architecture used to replicate the information from the κ -maps and relies on different multiscale levels to learn the non-Gaussian information. In Figure 1 we describe this architecture, highlighting the different multiscale transforms. These are based on several invertible coupling layers, squeezing, and splitting operations defined in [48] to create a multiscale flow that generates the target distribution from pure Gaussian noise. In total, several squeeze layers and split layers for maps with sizes of 64×64 , 128×128 and, 256×256 pixels (one color Chanel), resulting in several resolution map representations. When applying the coupling layers, a convolutional neural network (CNN) is used to learn the coefficients of the affine transformation. After all the transformation have been applied, the original image is taken to a latent space representing pure Gaussian noise. Once trained, the reverse process starts from the noise field at the same resolution, turning to a confident κ -map with the same pixel distribution as the original maps. To train flow-based models, the loss function is based on the Kullback-Leibler (KL) divergence, which serves to minimize the distance between the distribution modeled by the flow and the proposed (Gaussian) prior. For the objective of learning the pixel distribution of convergence maps, we study multiscale architectures with different sizes: A simple architecture is composed of 518K parameters (MS1), and adding additional multiscale layers results in 665K parameters (MS2). For larger

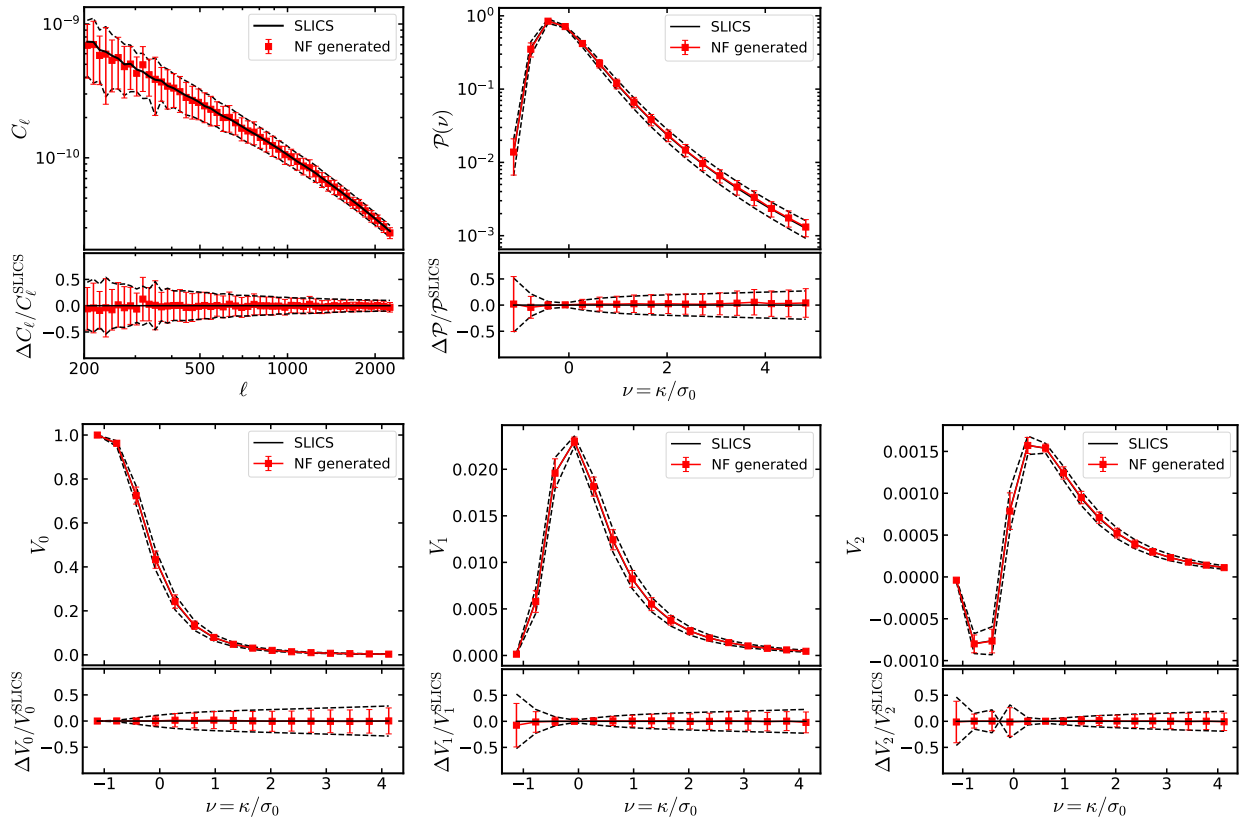


FIG. 2. Replication of summary statistics using NF network and SLICS simulations (ground truth) dataset. We calculate the mean of the angular power spectrum $C_\ell^{\kappa\kappa}$, κ -PDF (top panels) and three Minkowski functionals V_0 , V_1 and V_2 (bottom panels) for the SLICS simulation (black lines) and the synthetic data vectors generated using the Neural Spline Flow network. The bottom sub-panels include the relative difference compared to the ground truth data vector. We add the standard deviation of SLICS (black dashed lines) and the synthetic data (red error bars).

images (256×256), we use a multiscale architecture with 893K parameters (MS3).

V. RESULTS

A. Replicating C_ℓ and non-Gaussian statistics

We first examine the replication of summary statistics using the NSF network trained on the individual data vectors corresponding to the different summary statistics. Figure 2 presents a comparison between the angular power spectrum $C_\ell^{\kappa\kappa}$, the κ -PDF, and the Minkowski functionals (MFs) computed from the SLICS simulations and those reproduced by the trained NSF model. The results show a close agreement with the ground truth, with differences typically below the 1% level across different binning schemes in ℓ -multipoles and normalized field values ν . Both the mean and standard deviation are shown in Figure 2, demonstrating that the network successfully learns these statistical properties directly from the binned distributions of each summary statistic.

We show in Figure 3 the ratio of covariances between

the NF-generated and simulated datasets for each summary statistic. In the case of the covariance comparison, we focus primarily on the off-diagonal components and compute their relative values as $\rho' = \sqrt{C_{ij}^{\text{NF}} / C_{ij}^{\text{Sim}}}$, where C_{ij}^{NF} denotes the covariance of the summary statistic generated by the NF network, and C_{ij}^{Sim} represents the corresponding covariance from the SLICS simulations. We adopt this definition instead of the classical correlation coefficient, $\rho = C_{ij} / \sqrt{C_{ii} C_{jj}}$, to avoid normalizing by the diagonal elements, which could mask small differences if the variances differ between datasets. The quantity ρ'_{ij} provides a more direct measure of deviations related to the standard deviation, consistent with the quantities shown in the lower panels of Figure 2. This choice facilitates the interpretation of fractional differences in the covariance structure.

Figure 3 shows that the off-diagonal terms of the covariance are underestimated by the network by approximately 5% for $C_\ell^{\kappa\kappa}$ and the PDF, and by about 10% for the MFs, as indicated by the light-blue colors. Some of these values might be expected, as some of the statistics are divided into several data bins, such as $C_\ell^{\kappa\kappa}$, making the covariance be more sensitive to sampling noise.

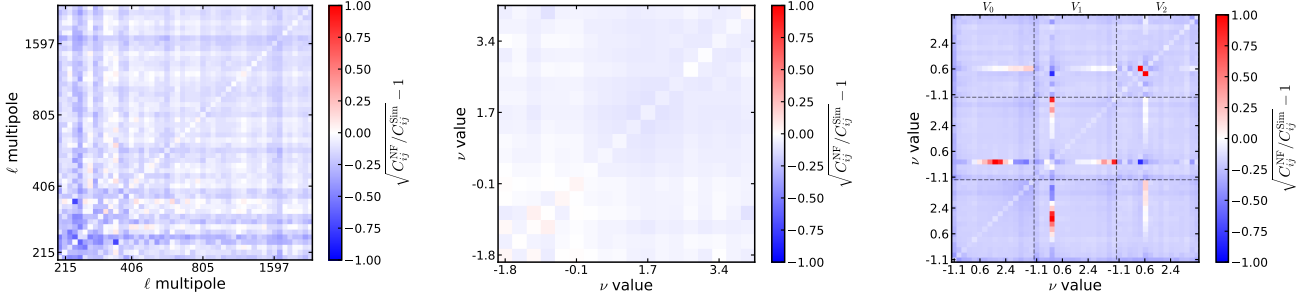


FIG. 3. Ratio of the covariance matrix of the summary statistic showed in Fig. 2, C_ℓ^{KK} (left), κ -PDF (middle), and Minkowski functionals (right) for NF generated data vectors and SLIC simulations.

Overall, these values remain stable across the different binnings of ℓ -multipoles and normalized field values ν tested for the data vectors. The accuracy, however, decreases slightly for configurations with $N_{\ell\text{-bins}} > 50$ and $N_{\nu\text{-bins}} > 20$.

B. Statistic of NF generated κ -maps

The next step is to test whether, beyond reproducing the information contained in the summary statistics of the simulations, NF networks can also replicate complete κ -maps by learning the distribution of individual pixels. In this case, square images of size $N \times N$ pixels are passed through the flow and transformed into Gaussian noise images of identical dimensions. Once trained, the inverse flow generates new realizations of the convergence field from any initial Gaussian random field. As the dimensionality of the problem increases rapidly with the image size (scaling as N^2), in contrast to the previous case based on one-dimensional data vectors, we adopt the MS flow architecture. This design improves the performance by introducing convolution-like transformations that efficiently capture spatial correlations within the maps. To evaluate how the network results vary with image size, we test three resolutions. Figure 4 presents results for three different map sizes: $N_{\text{pix},1} = 64 \times 64$, $N_{\text{pix},2} = 128 \times 128$, and $N_{\text{pix},3} = 256 \times 256$. Because the different resolutions probe distinct angular scales, they correspond to different ranges in angular scale, represented by a range of ℓ multipoles. We limit the comparison of the replicated power spectrum to the range $200 < \ell < 1100$, determined by the image resolution and map size.

For the selected range, the mean of the power spectrum C_ℓ^{KK} is recovered with percent-level accuracy, within approximately 3% of the ground truth estimated from the SLICS simulations and consistent within one standard deviation. However, the standard deviation of the power spectrum is systematically underestimated for the NF-generated maps. This underestimation is also evident in the covariance matrices of the power spectrum shown in Figure 5, where an excess of blue regions indicates lower values relative to the simulations. The accuracy with

which the covariance terms are recovered ρ' decreases with increasing map size, becoming most pronounced for $N_{\text{pix},3}$, where even the variance (diagonal terms) is at least 25% smaller than the ground truth. We attribute this loss of accuracy to the rapid increase in dimensionality with image size, when using the MS1 model only. This trend is clearly observed as both the variance and covariance accuracy degrade with higher dimensionality, reaching discrepancies up to 75% for the largest maps ($N_{\text{pix},3}$).

C. Network size, data augmentation, and noise

To assess whether the NF-generated maps can reproduce the same statistical properties as those computed from the simulations, we evaluate how well the network architecture handles the increased dimensionality of the κ -map images. We explore three strategies: increasing the network size, applying data augmentation during training, and adding stochastic noise to the training samples.

First, we extend the depth of the multiscale (MS) flow architecture described in Section IV. Specifically, we introduce two additional levels of squeeze-and-split operations within the flow, which enable the network to better capture multi-scale structure in the input maps. This approach has been shown by Dai and Seljak [23] to enhance the performance of flow-based models in replicating weak-lensing images. Our implementation includes three multiscale levels in total, with additional coupling layers inserted at each level following the RealNVP architecture of Dinh *et al.* [48]. This design allows the network to efficiently learn spatial correlations across multiple resolutions.

We also implement a data augmentation framework to make more efficient use of the limited number of simulated κ -maps available for training. Following a procedure similar to that of Ribli *et al.* [50], we modify the original images to expand the effective training set. Starting from the $10 \times 10 \text{ deg}^2$ SLICS maps, we randomly select a subset of maps and crop square regions of $5 \times 5 \text{ deg}^2$, which are then randomly rotated by 90° or 180° . This

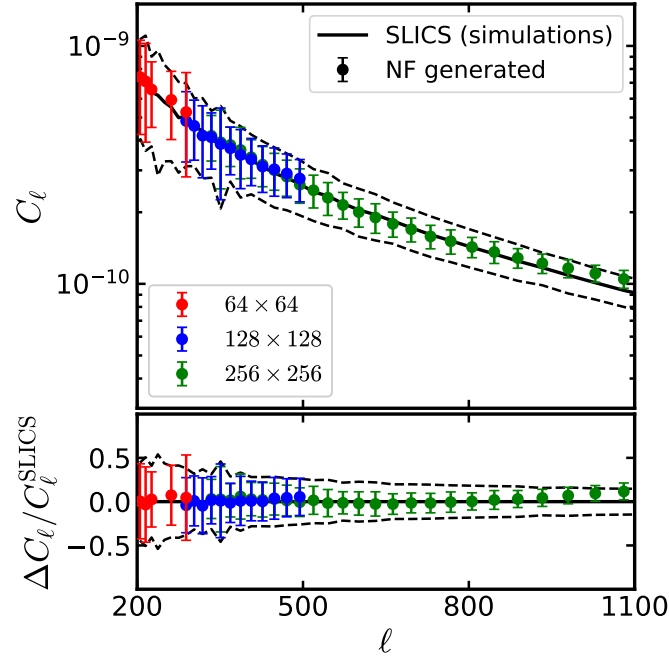


FIG. 4. Angular Power spectrum $C_\ell^{\kappa\kappa}$ of NF generated convergence maps compared to the κ -maps from SLICS simulations. These are calculated from maps with different pixel sizes: 64×64 (red), 128×128 (blue), and 256×256 green. We add the relative difference w.r.t. the ground truth in the bottom panel.

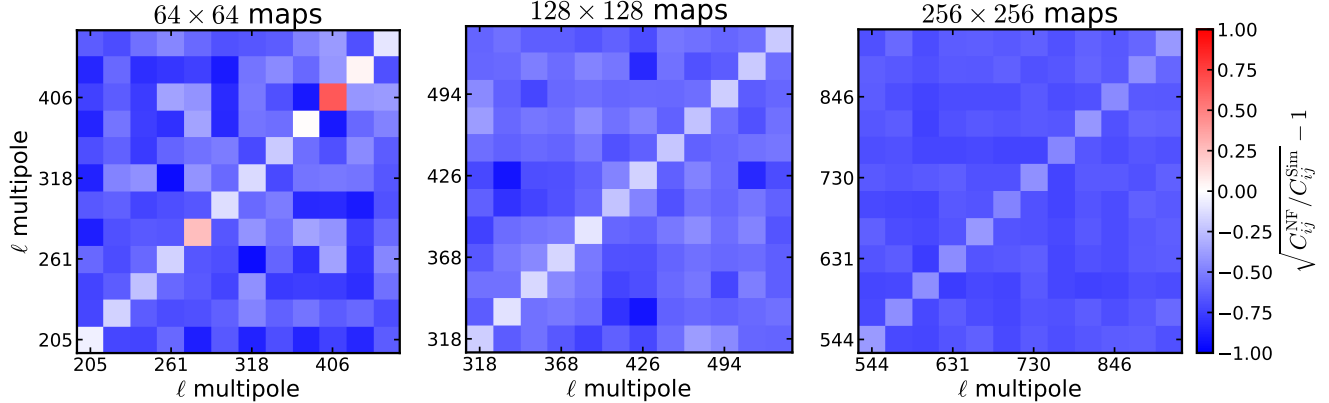


FIG. 5. Ratio of covariance for $C_\ell^{\kappa\kappa}$ in Fig. 4. We select 12 bins for each resolution map to help the comparison between the cases: 64×64 (left), 128×128 (middle), and 256×256 right.

process increases the number of training samples without altering the statistical properties of the replicated summary statistics, which are rotationally invariant. However, it helps the network to include more images during the training process. It also exposes the network to a broader variety of local features during training. The selection of this subsample is done in order to artificially increase the variance of the training set. Although this may slightly change the target power spectrum, as we remove the large modes outside the 5 deg window, previous studies [51–53] have shown that the mean of the summary statistics can be accurately captured using only a frac-

tion of the original sample. We maintain the same ranges of multipole scales and normalized field values ν , as these are confidently represented by the summary statistics derived from both the 10 deg and 5 deg aperture maps. In addition, we generate a complementary dataset of noisy images by adding Gaussian noise with a standard deviation of $\sigma_\kappa = 0.008$, chosen to approximate an LSST-like survey. We treat this as an independent augmentation case, since the addition of noise is expected to affect the summary statistics while also acting as an effective regularization technique during training [54, 55].

Figure 6 presents the summary statistics obtained from

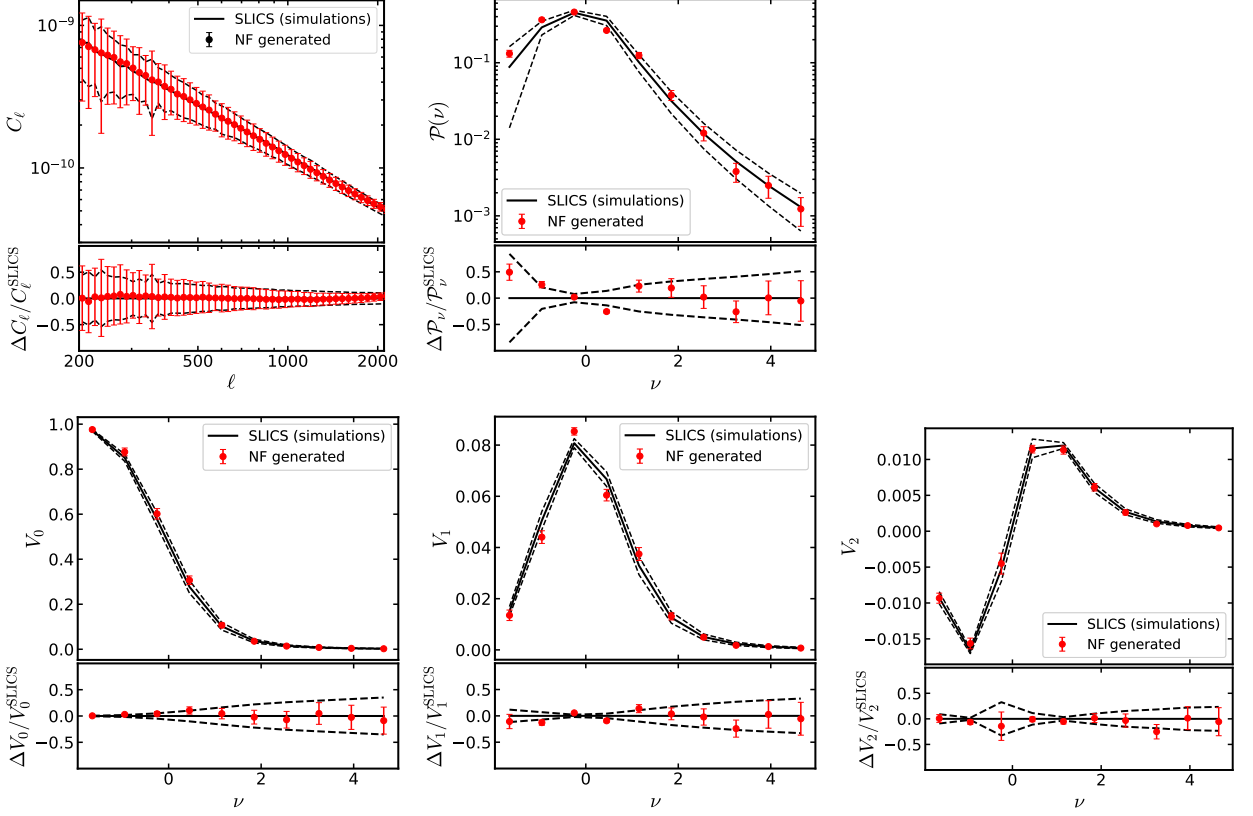


FIG. 6. Same as Figure 2 but with NF generated maps using the multiscale architecture. We calculate the summary statistics using κ -maps with included pixel noise σ_κ .

the NF-generated κ -maps. For this analysis, we generate 4000 maps with an angular size of $5 \times 5 \text{ deg}^2$ and apply a Gaussian smoothing filter with a 2 arcmin kernel to compute both the PDF and MFs. These results show an improvement in the recovery of the mean and standard deviation of the power spectrum compared to the 256×256 -pixel map results shown in Figure 4. For C_ℓ even though the variance is slightly overestimated for large multipole values $l < 500$ these allow us to correct for the previously underestimated variance (and covariance) terms at $l > 500$. Similar for PDF and MFs results, the results agree with the mean of simulation measurements, however still showing a underestimated variance in some ν bins. The partial improvement arises from the combination of the studied factors: a larger network architecture with additional multiscale levels, the inclusion of data augmentation in the training set, and the addition of Gaussian noise to the maps during training. Particularly, the addition of noise helps to capture the small-scale variability and yield a more accurate replication of the statistical properties of the weak-lensing convergence field.

The comparison between the replicated and simulated covariance matrices is shown in Figure 7. We separately assess the effects of increasing the network size, applying data augmentation, and adding pixel noise during train-

ing. Overall, both enlarging the network and augmenting the training data improve the recovery of the covariance structure, although the off-diagonal elements remain underestimated by approximately 10% relative to the simulation covariances. Introducing pixel noise during training further enhances performance, reducing the average discrepancy of the off-diagonal terms to about 5% with $\rho' - 1$ close to zero. We repeat the covariance analysis for the κ -PDF and MFs in Figure 8, which display similar trends but with lower accuracy overall. In summary, these results indicate that the accuracy of the replicated summary statistics improves when the network is trained on noisy maps, suggesting that the model is capable of learning the convergence signal when extra stochasticity is added to the training sample.

Finally, we evaluate the accuracy of the off-diagonal covariance terms as a function of the number of simulations included in the training set, as shown in Figure 9. By varying the number of simulations used to construct the training data, we aim to achieve two objectives: to artificially increase the variance by training on a random subsample of the original dataset, while preserving the mean, since only a few realizations ($\mathcal{O}(100)$) are sufficient to estimate the mean power spectrum accurately. And, to examine how the covariance accuracy behaves for smaller training sets. The results in Figure 9 indicate that using

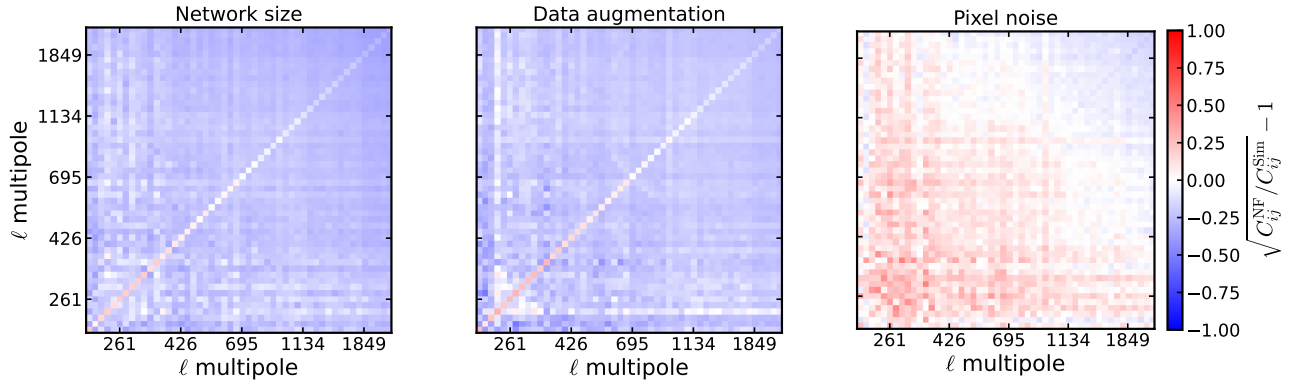


FIG. 7. $C_{\ell}^{\kappa\kappa}$ covariance of NF generated maps for different training cases: Using a larger network size for training with κ -maps (left), using data augmentation of the sample (middle), and adding pixel noise to the samples when training (right). The color bar coding is the same as in Figure 3

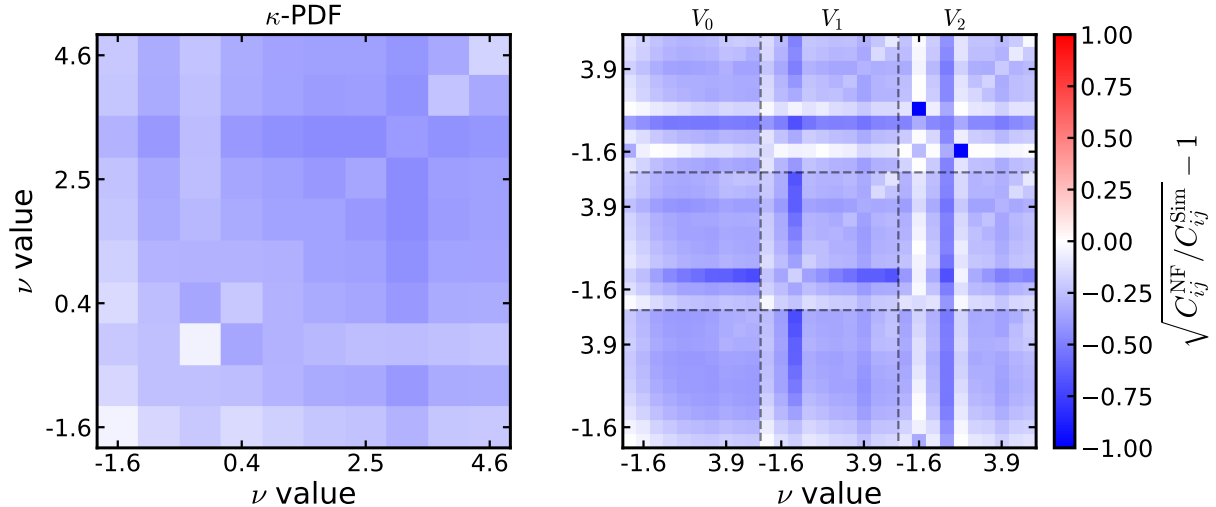


FIG. 8. Same as in 7 (noisy data maps), but for PDF and MF covariance.

approximately 100 simulations is sufficient to reproduce the SLICS covariance with an average accuracy of about 92% in the off-diagonal elements, for a $C_{\ell}^{\kappa\kappa}$ like the one in Figure 6. The accuracy decreases as the number of simulations in the subsample increases, reaching values of $\sim 86\%$. Conversely, when the number of simulations approaches the full sample ($\mathcal{O}(1000)$), the accuracy rises again, as the network learns the full distribution of the dataset and therefore recovers a more representative covariance. Nevertheless, even in this case the accuracy remains close to 90%, suggesting that the off-diagonal covariance is slightly underestimated even when the network is trained on the complete set of maps. It is useful to note that for small numbers of training simulations, the network is relatively undertrained in comparison to a full sample and has not yet captured the intrinsic variability of the convergence fields. In this regime, the stochasticity in the generated maps arising can introduce an additional

scatter that artificially inflates the apparent covariance, partially compensating for the true underestimation of the off-diagonal terms. As the size of the training set increases, the scatter is reduced as the network predictions become more stable. In the limit of very small training sets, this effect can be understood by considering the network effectively untrained. Only when the network is trained on a sufficiently large fraction of the full simulation suite does it begin to accurately learn the full data distribution, at which point the recovered covariance converges toward its true value.

VI. CONCLUSIONS

In this paper, we study the replication of a set of summary statistics of the convergence field using normalizing flow neural networks. To understand how di-

dimensionality affects these measurements, we test the NF generated data at two levels: the summary statistics level and the map level.

For the first level, by using a simple architecture based on the neural spline flow network, the summary statistics are replicated accurately at the percentage level, for the mean and standard deviation (variance). For covariance, the accuracy is close to 5-10% but depends on the type of summary statistics and the dimensionality of the data vector. We find $C_{\ell}^{\kappa\kappa}$ calculated in up to 50 log-separated ℓ multipole bins, and κ -PDF and MF binned in 20 ν bins recover the statistics more accurately ($\mathcal{O}(1\%)$). However, we find that once the dimensionality of the data vector to replicate increases, the accuracy the covariance is largely underestimated, for a fixed network size ($\mathcal{O}(10\%)$).

For the second level, where we train directly on the κ -maps instead of the summary statistics. We show that for the small multiscale network, with one squeeze and split transformation, the results lack the correct replication of the $C_{\ell}^{\kappa\kappa}$ variance and covariance by around 25% and 50%. The effect increases when using larger maps and keeping the network fixed, suggesting more multiscale layers are needed. To improve the accuracy performance, we increased the size of the multiscale architecture to incorporate the learning of different scales. By increasing the network size, and adding more scale transformations (MS3), the accuracy of the variance and covariance is recovered at 10% level. Similar effect is obtained when using data augmentation to increase the size of the training set, recovering the covariance off-diagonal coefficients with accuracy of 15%. The accuracy of the mean, variance and covariance of the summary statistics is largely improved once a noisy data is added to the training set, leading to a 5% accuracy in the off-diagonal terms for the covariance of the replicated power spectrum. For PDF and MF, NF networks reach $\approx 10\%$ accuracy for statistics and covariance.

These findings are still consistent with previous applications of machine learning to weak lensing, which demonstrate the potential of generative models—such as GANs, VAEs, and normalizing flows [21, 30, 56–58] to replicate non-Gaussian features of convergence fields and enable fast map generation. However, we emphasize how the limited information used for training can compromise the accuracy of the off-diagonal terms of the covariance for different summary statistics, indicating that further steps must be taken before using generated maps for cosmological inference, as underestimated covariance can lead to overconfident contours. A simple explanation for this behavior is the poor scaling of NF networks when a limited sample of simulations is used when train high-dimensional maps. This suggests that the sub-arcmin Requirements of stage-IV weak lensing surveys require large models, with an effective understanding of noise and data augmentation techniques, as shown in different studies [55, 59]. In particular, diffusion model architec-

tures [26], where the κ signal and pixel noise must be disentangled, can benefit from these data augmentation

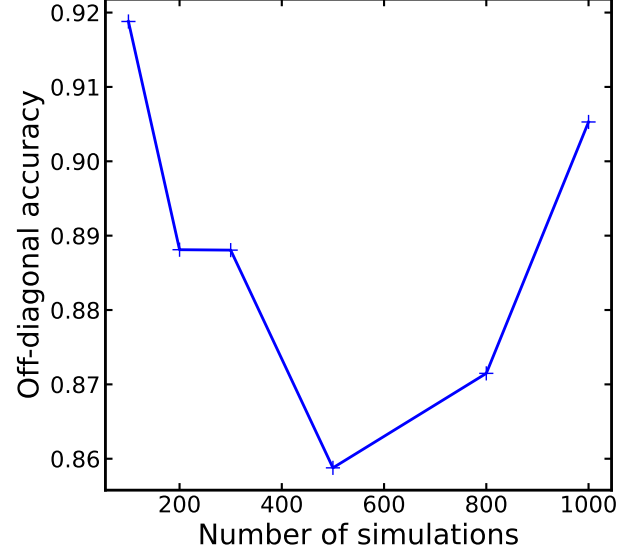


FIG. 9. Accuracy of the off-diagonal covariance terms of the convergence power spectrum $C_{\ell}^{\kappa\kappa}$ measured from normalizing-flow (NF)-generated maps, as a function of the number of simulations used for training. We construct six independent samples containing 100, 200, 300, 500, 800, and 954 simulations used to generate a training set, and compare the resulting covariance estimates to those obtained from the full SLICS simulation suite. The accuracy is computed by averaging the off-diagonal covariance elements over the ℓ bins used to estimate $C_{\ell}^{\kappa\kappa}$, since these terms are approximately scale-independent across multipoles. The diagonal elements (variances) are excluded to isolate and quantify potential underestimation of the off-diagonal covariance.

techniques. Our work shows that the NF performance can be mitigated by data augmentation techniques.

ACKNOWLEDGMENTS

JA acknowledges useful discussions with Ben Horowitz and Linda Blot. We thank Joachim Harnois-Déraps for providing the SLICS simulations. JA is supported by JSPS KAKENHI Grant JP23K19064. LT is supported by JSPS KAKENHI Grant 24K22878. JL is supported by JSPS KAKENHI Grants 23H00107, 25H00403. We acknowledge the Texas Advanced Computing Center (TACC) at The University of Texas at Austin for providing grid resources that have contributed to our work, including the Anvil machine for GPU computation. This research used computing resources at Kavli IPMU. The Kavli IPMU is supported by the WPI (World Premier International Research Center) Initiative of the MEXT (Japanese Ministry of Education, Culture, Sports, Science and Technology).

[1] M. Bartelmann and P. Schneider, *Physics Reports* **340**, 291 (2001).

[2] M. Kilbinger, *Reports on Progress in Physics* **78**, 086901 (2015).

[3] R. Mandelbaum, *Annual Review of Astronomy and Astrophysics* **56**, 393 (2018).

[4] D. Huterer, *General Relativity and Gravitation* **42**, 2177–2195 (2010).

[5] D. Huterer and D. L. Shafer, *Reports on Progress in Physics* **81**, 016901 (2018), arXiv:1709.01091 [astro-ph.CO].

[6] A. e. a. Amon, *Physical Review D* (2022).

[7] C. Heymans, T. Tröster, M. Asgari, C. Blake, H. Hildebrandt, B. Joachimi, K. Kuijken, C.-A. Lin, A. G. Sánchez, J. L. van den Busch, A. H. Wright, A. Amon, M. Bilicki, J. de Jong, M. Crocce, A. Dvornik, T. Erben, M. C. Fortuna, F. Getman, B. Giblin, K. Glazebrook, H. Hoekstra, S. Joudaki, A. Kannawadi, F. Köhlinger, C. Lidman, L. Miller, N. R. Napolitano, D. Parkinson, P. Schneider, H. Shan, E. A. Valentijn, G. Verdoes Kleijn, and C. Wolf, *A&A* **646**, A140 (2021), arXiv:2007.15632 [astro-ph.CO].

[8] C. e. a. Hikage, *Publications of the Astronomical Society of Japan* **71**, 43 (2019).

[9] R. e. a. Laureijs, *Euclid Definition Study Report*, Tech. Rep. 2011-12 (ESA/SRE, 2011).

[10] L. S. Collaboration, *LSST Science Book, Version 2.0*, Tech. Rep. (Rubin Observatory, 2009) arXiv:0912.0201.

[11] N. Kaiser and G. Squires, *The Astrophysical Journal* **404**, 441 (1993).

[12] R. e. a. Takahashi, *The Astrophysical Journal* **850**, 24 (2017).

[13] C. Vale and M. White, *ApJ* **592**, 699 (2003), arXiv:astro-ph/0303555 [astro-ph].

[14] S. Pires, J. L. Starck, A. Amara, R. Teyssier, A. Réfrégier, and J. Fadili, *MNRAS* **395**, 1265 (2009), arXiv:0804.4068 [astro-ph].

[15] N. e. a. Jeffrey, *Monthly Notices of the Royal Astronomical Society* **505**, 4626 (2021).

[16] R. Massey, H. Hoekstra, T. Kitching, J. Rhodes, M. Cropper, J. Amiaux, D. Harvey, Y. Mellier, M. Meneghetti, L. Miller, S. Paulin-Henriksson, S. Pires, R. Scaramella, and T. Schrabback, *MNRAS* **429**, 661 (2013), arXiv:1210.7690 [astro-ph.CO].

[17] J. Harnois-Déraps et al., *Monthly Notices of the Royal Astronomical Society* **481**, 1337 (2018).

[18] T. Tröster, C. Ferguson, J. Harnois-Déraps, and I. G. McCarthy, *MNRAS* **487**, L24 (2019), arXiv:1903.12173 [astro-ph.CO].

[19] A. C. Rodríguez, T. Kacprzak, A. Lucchi, A. Amara, R. Sgier, J. Fluri, T. Hofmann, and A. Réfrégier, *Computational Astrophysics and Cosmology* **5**, 4 (2018), arXiv:1801.09070 [astro-ph.CO].

[20] S. e. a. Ravanbakhsh, *Proceedings of the 34th International Conference on Machine Learning* (2017).

[21] M. Mustafa, D. Bard, W. Bhimji, Z. Lukić, R. Al-Rfou, and J. M. Kratochvil, *Computational Astrophysics and Cosmology* **6**, 1 (2019), arXiv:1706.02390 [astro-ph.IM].

[22] J. Fluri, T. Kacprzak, A. Lucchi, A. Amara, et al., *Physical Review D* **100**, 063514 (2019).

[23] B. Dai and U. Seljak, in *Machine Learning for Astrophysics* (2023) p. 10, arXiv:2306.04689 [astro-ph.CO].

[24] J. Whitney, T. Liaudat, M. Price, M. Mars, and J. D. McEwen, arXiv e-prints , arXiv:2406.15424 (2024), arXiv:2406.15424 [astro-ph.CO].

[25] J. J. Whitney, T. I. Liaudat, M. A. Price, M. Mars, and J. D. McEwen, arXiv e-prints , arXiv:2410.24197 (2024), arXiv:2410.24197 [astro-ph.CO].

[26] S. S. Boruah, M. Jacob, and B. Jain, *Phys. Rev. D* **111**, 083542 (2025), arXiv:2502.04158 [astro-ph.CO].

[27] A. Gupta, J. M. Z. Matilla, D. Hsu, and Z. Haiman, *Phys. Rev. D* **97**, 103515 (2018).

[28] N. Perraudeau, S. Marcon, A. Lucchi, and T. Kacprzak, arXiv e-prints , arXiv:2004.08139 (2020), arXiv:2004.08139 [astro-ph.CO].

[29] F. e. a. Villaescusa-Navarro, *The Astrophysical Journal* **915**, 71 (2021).

[30] B. Dai and U. Seljak, *MNRAS* **516**, 2363 (2022), arXiv:2202.05282 [astro-ph.CO].

[31] A. Amon et al., *Physical Review D* **105**, 023520 (2022).

[32] M. Asgari et al., *Astronomy & Astrophysics* **645**, A104 (2021).

[33] C. Hikage et al., *Publications of the Astronomical Society of Japan* **71**, 43 (2019).

[34] D. Munshi and B. Jain, *MNRAS* **318**, 109 (2000), arXiv:astro-ph/9911502 [astro-ph].

[35] A. Petri, *Physical Review D* **94**, 063534 (2016).

[36] M. Gatti, B. Jain, C. Chang, M. Raveri, D. Zürcher, L. Secco, L. Whiteway, N. Jeffrey, C. Doux, T. Kacprzak, D. Bacon, P. Fosalba, A. Alarcon, A. Amon, K. Bechtol, M. Becker, G. Bernstein, J. Blazek, A. Campos, A. Choi, C. Davis, J. Derose, S. Dodelson, F. Elsner, J. Elvin-Poole, S. Everett, A. Ferte, D. Gruen, I. Harrison, D. Huterer, M. Jarvis, E. Krause, P. F. Leget, P. Lemos, N. MacCrann, J. McCullough, J. Muir, J. Myles, A. Navarro, S. Pandey, J. Prat, R. P. Rollins, A. Roodman, C. Sanchez, E. Sheldon, T. Shin, M. Troxel, I. Tutasaus, B. Yin, M. Aguena, S. Allam, F. Andrade-Oliveira, J. Annis, E. Bertin, D. Brooks, D. L. Burke, A. Carnero Rosell, M. Carrasco Kind, J. Carretero, R. Cawthon, M. Costanzi, L. N. da Costa, M. E. S. Pereira, J. De Vicente, S. Desai, H. T. Diehl, J. P. Dietrich, P. Doel, A. Drlica-Wagner, K. Eckert, A. E. Evrard, I. Ferrero, J. García-Bellido, E. Gaztanaga, T. Giannantonio, R. A. Gruendl, J. Gschwend, G. Gutierrez, S. R. Hinton, D. L. Hollowood, K. Honscheid, D. J. James, K. Kuehn, N. Kuropatkin, O. Lahav, C. Lidman, M. A. G. Maia, J. L. Marshall, P. Melchior, F. Menanteau, R. Miquel, R. Morgan, A. Palmese, F. Paz-Chinchón, A. Pieres, A. A. Plazas Malagón, K. Reil, M. Rodriguez-Monroy, A. K. Romer, E. Sanchez, M. Schubnell, S. Serrano, I. Sevilla-Noarbe, M. Smith, M. Soares-Santos, E. Suchyta, G. Tarle, D. Thomas, C. To, T. N. Varga, and DES Collaboration, *Phys. Rev. D* **106**, 083509 (2022), arXiv:2110.10141 [astro-ph.CO].

[37] C. Uhlemann, O. Friedrich, F. Villaescusa-Navarro, A. Banerjee, and S. Codis, *MNRAS* **495**, 4006 (2020), arXiv:1911.11158 [astro-ph.CO].

[38] L. Thiele, G. A. Marques, J. Liu, and M. Shirasaki, *Phys. Rev. D* **108**, 123526 (2023).

[39] L. Castiblanco, C. Uhlemann, J. Harnois-Déraps, and

A. Barthelemy, The Open Journal of Astrophysics **7**, 59 (2024), arXiv:2405.09651 [astro-ph.CO].

[40] J. M. Kratochvil, E. A. Lim, and S. Wang, Physical Review D **85**, 103513 (2012).

[41] D. Munshi *et al.*, Monthly Notices of the Royal Astronomical Society **419**, 536 (2012).

[42] J. Armijo, G. A. Marques, C. P. Novaes, L. Thiele, J. A. Cowell, D. Grandón, M. Shirasaki, and J. Liu, Monthly Notices of the Royal Astronomical Society, staf257 (2025), <https://academic.oup.com/mnras/advance-article-pdf/doi/10.1093/mnras/staf257/61870752/staf257.pdf>.

[43] G. A. Marques, J. Liu, M. Shirasaki, L. Thiele, D. Grandón, K. M. Huffenberger, S. Cheng, J. Harnois-Déraps, K. Osato, and W. R. Coulton, MNRAS **528**, 4513 (2024), arXiv:2308.10866 [astro-ph.CO].

[44] S. Cheng, G. A. Marques, D. Grandón, L. Thiele, M. Shirasaki, B. Ménard, and J. Liu, arXiv e-prints, arXiv:2404.16085 (2024), arXiv:2404.16085 [astro-ph.CO].

[45] C. P. Novaes, L. Thiele, J. Armijo, S. Cheng, J. A. Cowell, G. A. Marques, E. G. M. Ferreira, M. Shirasaki, K. Osato, and J. Liu, Phys. Rev. D **111**, 083510 (2025), arXiv:2409.01301 [astro-ph.CO].

[46] C. Durkan, A. Bekasov, I. Murray, and G. Papamakarios, arXiv e-prints, arXiv:1906.04032 (2019), arXiv:1906.04032 [stat.ML].

[47] G. Papamakarios, T. Pavlakou, and I. Murray, arXiv e-prints, arXiv:1705.07057 (2017), arXiv:1705.07057 [stat.ML].

[48] L. Dinh, J. Sohl-Dickstein, and S. Bengio, arXiv e-prints, arXiv:1605.08803 (2016), arXiv:1605.08803 [cs.LG].

[49] D. P. Kingma and P. Dhariwal, arXiv e-prints, arXiv:1807.03039 (2018), arXiv:1807.03039 [stat.ML].

[50] D. Ribli, B. Á. Pataki, J. M. Zorrilla Matilla, D. Hsu, Z. Haiman, and I. Csabai, MNRAS **490**, 1843 (2019), arXiv:1902.03663 [astro-ph.CO].

[51] A. C. Pope and I. Szapudi, MNRAS **389**, 766 (2008), arXiv:0711.2509 [astro-ph].

[52] A. Petri, Z. Haiman, and M. May, Phys. Rev. D **93**, 063524 (2016), arXiv:1601.06792 [astro-ph.CO].

[53] D. W. Pearson and L. Samushia, Monthly Notices of the Royal Astronomical Society **457**, 993 (2016), <https://academic.oup.com/mnras/article-pdf/457/1/993/18169038/stw062.pdf>.

[54] M. Shirasaki, N. Yoshida, and S. Ikeda, Phys. Rev. D **100**, 043527 (2019).

[55] K. Zhong, M. Gatti, and B. Jain, Phys. Rev. D **110**, 043535 (2024), arXiv:2403.01368 [astro-ph.CO].

[56] S. S. Boruah, P. Fiedorowicz, R. Garcia, W. R. Coulton, E. Rozo, and G. Fabbian, arXiv e-prints, arXiv:2406.05867 (2024), arXiv:2406.05867 [astro-ph.CO].

[57] M. Shirasaki and S. Ikeda, The Open Journal of Astrophysics **7**, 42 (2024), arXiv:2310.17141 [astro-ph.CO].

[58] S. D. Aoyama, K. Osato, and M. Shirasaki, arXiv e-prints, arXiv:2505.00345 (2025), arXiv:2505.00345 [astro-ph.CO].

[59] M. Shirasaki, K. Moriwaki, T. Oogi, N. Yoshida, S. Ikeda, and T. Nishimichi, MNRAS **504**, 1825 (2021), arXiv:1911.12890 [astro-ph.CO].